

# Compressive Deconvolution in Medical Ultrasound Imaging

Zhouye Chen, Adrian Basarab, Denis Kouamé

## Abstract

The interest of compressive sampling in ultrasound imaging has been recently extensively evaluated by several research teams. Following the different application setups, it has been shown that the RF data may be reconstructed from a small number of measurements and/or using a reduced number of ultrasound pulse emissions. Nevertheless, RF image spatial resolution, contrast and signal to noise ratio are affected by the limited bandwidth of the imaging transducer and the physical phenomenon related to US wave propagation. To overcome these limitations, several deconvolution-based image processing techniques have been proposed to enhance the ultrasound images. In this paper, we propose a novel framework, named compressive deconvolution, that reconstructs enhanced RF images from compressed measurements. Exploiting an unified formulation of the direct acquisition model, combining random projections and 2D convolution, the benefit of our approach is the joint data volume reduction and image quality improvement. The proposed optimization method, based on the Alternating Direction Method of Multipliers, is evaluated on both simulated and *in vivo* data.

## Index Terms

Compressive sampling, deconvolution, ultrasound imaging, alternating direction method of multipliers

## I. INTRODUCTION

Ultrasound (US) medical imaging has the advantages of being noninvasive, harmless, cost-effective and portable over other imaging modalities such as X-ray Computed Tomography or Magnetic Resonance Imaging [1].

Despite its intrinsic rapidity of acquisition, several US applications such as cardiac, Doppler, elastography or 3D imaging may require higher frame rates than those provided by conventional acquisition

Zhouye Chen, Adrian Basarab and Denis Kouamé are with IRIT UMR CNRS 5505, University of Toulouse, Toulouse, France (e-mail: {zhouye.chen, adrian.basarab, denis.kouame }@irit.fr)

schemes (e.g. ultrafast imaging [2]) or may suffer from the high amount of acquired data. In this context, a few research teams have recently evaluated the application of compressive sampling (CS) to 2D and 3D US imaging (e.g. [3–8]) or to duplex Doppler [9]. CS is a mathematical framework allowing to recover, via non linear optimization routines, an image from few linear measurements (below the limit standardly imposed by the Shannon-Nyquist theorem) [10, 11]. The CS acquisition model is given by

$$\mathbf{y} = \Phi \mathbf{r} + \mathbf{n} \quad (1)$$

where  $\mathbf{y} \in \mathbb{R}^M$  corresponds to the  $M$  compressed measurements of the image  $\mathbf{r} \in \mathbb{R}^N$  (one US radiofrequency (RF) image in our case),  $\Phi \in \mathbb{R}^{M \times N}$  represents the CS acquisition matrix composed for example of  $M$  random Gaussian vectors with  $M \ll N$  and  $\mathbf{n} \in \mathbb{R}^M$  stands for a zero-mean additive white Gaussian noise.

The CS theory demonstrates that the  $N$  pixels of image  $\mathbf{r}$  may be recovered from the  $M$  measurements in  $\mathbf{y}$  provided two conditions: i) the image must have a sparse representation in a known basis or frame and ii) the measurement matrix and sparsifying basis must be incoherent [12]. In US imaging, it has been shown that RF images may be recovered based on their sparsity in basis such as 2D Fourier [4], wavelets [8], waveatoms [7] or learning dictionaries [13], on Bernoulli Gaussian [14] or  $\alpha$ -stable statistical assumptions [15] and using various acquisition schemes such as plane-wave [8], Xampling [5] or projections on Gaussian [3] or Bernoulli random vectors [4].

However, the existing methods of CS in US have been shown to be able to recover images with a quality at most equivalent to those acquired using standard schemes. Nevertheless, the spatial resolution, the signal-to-noise ratio and the contrast of standard US images ( $\mathbf{r}$  in eq. (1)) are affected by the limited bandwidth of the imaging transducer, the physical phenomenon related to US wave propagation such as the diffraction and the imaging system. In order to overcome these issues, one of the research tracks extensively explored in the literature is the deconvolution of US images [16–20]. Based on the first order Born approximation, these methods assume that the US RF images follow a 2D convolution model between the point spread function (PSF) and the tissue reflectivity function (TRF), *i.e.* the image to be recovered [21]. Specifically, this results in  $\mathbf{r} = H\mathbf{x}$ , where  $H \in \mathbb{R}^{N \times N}$  is a block circulant with circulant block (BCCB) matrix related to the 2D PSF of the system and  $\mathbf{x} \in \mathbb{R}^N$  represents the lexicographically ordered tissue reflectivity function.

The objective of our paper is to propose a novel technique which is able to jointly achieve US data

volume reduction and image quality improvement. In other words, the main idea is to combine the two frameworks of CS and deconvolution applied to US imaging, resulting in the so-called compressive deconvolution (or CS deblurring) problem [22–26]. The combined direct model of joint CS and deconvolution is as follows:

$$\mathbf{y} = \Phi H \mathbf{x} + \mathbf{n} \quad (2)$$

where the variables  $\mathbf{y}$ ,  $\Phi$ ,  $H$ ,  $\mathbf{x}$  and  $\mathbf{n}$  have the same meaning as defined above. Inverting the model in (2) will allow us to estimate the TRF  $\mathbf{x}$  from the compressed RF measurements  $\mathbf{y}$ .

To our knowledge, our work is the first attempt of addressing the compressive deconvolution problem in US imaging. In the general-purpose image processing literature, a few methods have been already proposed aiming at solving (2) [22–28]. In [24, 27, 28], the authors assumed  $\mathbf{x}$  was sparse in the direct or image domain and the PSF was unknown. In [27, 28], a study on the number of measurements lower bound is presented, together with an algorithm to estimate the PSF and  $\mathbf{x}$  alternatively. The authors in [24] solved the compressive deconvolution problem using an  $\ell_1$ -norm minimization algorithm by making use of the "all-pole" model of the autoregressive process. In [22, 23],  $\mathbf{x}$  was considered sparse in a transformed domain and the PSF was supposed known. An algorithm based on Poisson singular integral and iterative curvelet thresholding was shown in [22]. The authors in [23] further combined the curvelet regularization with total variation to improve the performance in [22]. Finally, the methods in [25, 26] supposed the blurred signal  $\mathbf{r} = H\mathbf{x}$  was sparse in a transformed domain and the PSF unknown. They proposed a compressive deconvolution framework that relies on a constrained optimization technique allowing to exploit existing CS reconstruction algorithms.

In this paper, we propose a compressive deconvolution technique adapted to US imaging. Our solution is based on the alternating direction method of multipliers (ADMM) [29, 30] and exploits two constraints. The first one is related to CS and imposes via an  $\ell_1$ -norm the sparsity of the RF image  $\mathbf{r}$  in the transformed domain (Fourier domain, wavelet domain, etc). The second one imposes *a priori* information for the TRF  $\mathbf{x}$ . Gaussian and Laplacian statistics have been extensively explored in US imaging (see e.g. [17, 31, 32]). Moreover, recent results show that the Generalized Gaussian Distributed (GGD) is well adapted to model the TRF. Consequently, we employ herein the minimization of an  $\ell_p$ -norm of  $\mathbf{x}$ , covering all possible cases ranging from 1 to 2 [19, 20]. Similar to all existing frameworks, we consider the CS sampling matrix  $\Phi$  known. In US imaging, the PSF is unknown in practical applications. However, its estimation from the

RF data as an initialization step for the deconvolution has been extensively explored in US imaging. In this paper, we adopted the approach in [33] in order to estimate the PSF further used to construct the matrix  $H$ .

This paper is organized as follows. In section II, we formulate our problem as a convex optimization routine and propose an ADMM-based method to efficiently solve it. Supporting simulated and experimental results are provided in section III showing the contribution of our approach compared to existing methods and its efficiency in recovering the TRF from compressed US data. The conclusions are drawn in IV.

## II. PROPOSED ULTRASOUND COMPRESSIVE DECONVOLUTION ALGORITHM

### A. Optimization Problem Formulation

In order to estimate the TRF  $\mathbf{x}$  from the compressed and blurred measurements  $\mathbf{y}$ , an intuitive idea to invert the direct model in (2) is to proceed through two sequential steps. The aim of the first step is to recover the blurred US RF image  $\mathbf{r} = H\mathbf{x}$  from the compressed measurements  $\mathbf{y}$  by solving the following optimization problem:

$$\min_{\mathbf{a} \in \mathbb{R}^N} \|\mathbf{a}\|_1 + \frac{1}{2\mu} \|\mathbf{y} - \Phi\Psi\mathbf{a}\|_2^2 \quad (3)$$

where  $\mathbf{a}$  is the sparse representation of the US RF image  $\mathbf{r}$  in the transformed domain  $\Psi$ , that is,  $\mathbf{r} = H\mathbf{x} = \Psi\mathbf{a}$ . Different basis have been shown to provide good results in the application of CS in US imaging, such as wavelets, waveatoms or 2D Fourier basis [6]. In this paper the wavelets have been employed.

Once the blurred RF image is recovered by solving the convex problem in (3), one can use an US-dedicated deconvolution method to restore the TRF  $\mathbf{x}$ .

While the sequential approach represents the most intuitive way to solve the compressive deconvolution problem, dividing a single problem into two separate subproblems will inevitably generate larger estimation errors as shown by the results in section III. Therefore, we propose herein a method to solve the CS and deconvolution problem simultaneously, by reformulating our compressed deconvolution problem in:

$$\min_{\mathbf{x} \in \mathbb{R}^N} \|\Psi^{-1}H\mathbf{x}\|_1 + \alpha P(\mathbf{x}) + \frac{1}{2\mu} \|\mathbf{y} - \Phi H\mathbf{x}\|_2^2 \quad (4)$$

where  $P(\mathbf{x})$  is the regularization term employed for the TRF (supposed convex in this paper) and  $\alpha$  and  $\mu$  are standard hyperparameters balancing between the two regularization and data fidelity terms. Keeping in mind that the GGD prior has been recently shown to suitably model the TRF  $\mathbf{x}$  [19, 20], the US experiments will be done by assigning  $P(\mathbf{x})$  to  $\|\mathbf{x}\|_p^p$  for  $p$  between 1 and 2. However, in the next two paragraphs, the generic notation  $P(\mathbf{x})$  will be used in order to keep our approach as general as possible and adapt it if necessary for comparison purpose.

To solve the optimization problem in eq. (4), we propose hereafter an algorithm based on the alternating direction method of multipliers (ADMM).

### B. Basics of Alternating Direction Method of Multipliers

Before going into the details of our algorithm, we report in this paragraph the basics of ADMM. ADMM has been extensively studied in the areas of convex programming and variational inequalities, e.g., [29]. The general optimization problem considered in ADMM framework is as follows:

$$\begin{aligned} \min_{u,v} \quad & f(u) + g(v) \\ \text{s.t.} \quad & Bu + Cv = b, u \in \mathcal{U}, v \in \mathcal{V} \end{aligned} \tag{5}$$

where  $\mathcal{U} \subseteq \mathbb{R}^s$  and  $\mathcal{V} \subseteq \mathbb{R}^t$  are given convex sets,  $f : \mathcal{U} \rightarrow \mathbb{R}$  and  $g : \mathcal{V} \rightarrow \mathbb{R}$  are closed convex functions,  $B \in \mathbb{R}^{r \times s}$  and  $C \in \mathbb{R}^{r \times t}$  are given matrices and  $\mathbf{b} \in \mathbb{R}^r$  is a given vector.

By attaching the Lagrangian multiplier  $\lambda \in \mathbb{R}^r$  to the linear constraint, the Augmented Lagrangian (AL) function of (5) is

$$\begin{aligned} \mathcal{L}(u, v, \lambda) = & f(u) + g(v) - \lambda^t(Bu + Cv - b) \\ & + \frac{\beta}{2} \|Bu + Cv - b\|_2^2 \end{aligned} \tag{6}$$

where  $\beta > 0$  is the penalty parameter for the linear constraints to be satisfied. The standard ADMM framework follows the three steps iterative process:

$$\left\{ \begin{array}{l} u^{k+1} \in \underset{u \in \mathcal{U}}{\operatorname{argmin}} \mathcal{L}(u, v^k, \lambda^k) \\ v^{k+1} \in \underset{v \in \mathcal{V}}{\operatorname{argmin}} \mathcal{L}(u^{k+1}, v, \lambda^k) \\ \lambda^{k+1} = \lambda^k - \beta(Bu^{k+1} + Cv^{k+1} - b) \end{array} \right. \tag{7}$$

The main advantage of ADMM, in addition to the relative ease of implementation, is its ability to split awkward intersections and objectives to easy subproblems, resulting into iterations comparable to those of other first-order methods.

### C. Proposed ADMM parameterization for Ultrasound Compressive Deconvolution

In this subsection, we propose an ADMM method for solving the ultrasound compressive deconvolution problem in (4).

Using a trivial variable change, the minimization problem in (4) can be rewritten as:

$$\min_{\mathbf{x} \in \mathbb{R}^N} \|\mathbf{w}\|_1 + \alpha P(\mathbf{x}) + \frac{1}{2\mu} \|\mathbf{y} - A\mathbf{x}\|_2^2 \quad (8)$$

where  $\mathbf{a} = \Psi^{-1}H\mathbf{x}$ ,  $\mathbf{w} = \mathbf{a}$  and  $A = \Phi\Psi$ . Let us denote  $\mathbf{z} = \begin{bmatrix} \mathbf{w} \\ \mathbf{x} \end{bmatrix}$ . The reformulated problem in (8) can fit the general ADMM framework in (5) by choosing:  $f(\mathbf{a}) = \frac{1}{2\mu} \|\mathbf{y} - A\mathbf{a}\|_2^2$ ,  $g(\mathbf{z}) = \|\mathbf{w}\|_1 + \alpha P(\mathbf{x})$ ,  $B = \begin{bmatrix} I_N \\ \Psi \end{bmatrix}$ ,  $C = \begin{bmatrix} -I_N & \mathbf{0} \\ \mathbf{0} & -H \end{bmatrix}$  and  $\mathbf{b} = \mathbf{0}$ .  $I_N \in \mathbb{R}^{N \times N}$  is the identity matrix.

The augmented Lagrangian function of (8) is given by

$$\begin{aligned} \mathcal{L}(\mathbf{a}, \mathbf{z}, \boldsymbol{\lambda}) = & f(\mathbf{a}) + g(\mathbf{z}) - \boldsymbol{\lambda}^t(B\mathbf{a} + C\mathbf{z}) \\ & + \frac{\beta}{2} \|B\mathbf{a} + C\mathbf{z}\|_2^2 \end{aligned} \quad (9)$$

where  $\boldsymbol{\lambda} \in \mathbb{R}^{2N}$  stands for  $\boldsymbol{\lambda} = \begin{bmatrix} \boldsymbol{\lambda}_1 \\ \boldsymbol{\lambda}_2 \end{bmatrix}$ ,  $\boldsymbol{\lambda}_i \in \mathbb{R}^N$  ( $i = 1, 2$ ). According to the standard ADMM iterative scheme, the minimizations with respect to  $\mathbf{a}$  and  $\mathbf{z}$  will be performed alternatively, followed by the update of  $\boldsymbol{\lambda}$ .

### D. Regularization term for TRF

In this paper, we consider two regularization terms for the variable  $\mathbf{x}$ . The first one, although not adapted to US images, allows us to fairly compare our approach to the one proposed in [25]. Adapted to piece-wise constant images  $\mathbf{x}$ , the generalized total variation (TV) regularization term, used in [25], is given by:

$$P(\mathbf{x}) = \sum_{d \in D} 2^{1-o(d)} \sum_i |\Delta_i^d(\mathbf{x})|^p \quad (10)$$

where  $o(d) \in \{1, 2\}$  denotes the order of the difference operator  $\Delta_i^d(\mathbf{x})$ ,  $0 < p < 1$ , and  $d \in D = \{h, v, hh, vv, hv\}$ .  $\Delta_i^h(\mathbf{x})$  and  $\Delta_i^v(\mathbf{x})$  correspond, respectively, to the horizontal and vertical first order differences, at pixel  $i$ , that is,  $\Delta_i^h(\mathbf{x}) = u_i - u_{l(i)}$  and  $\Delta_i^v(\mathbf{x}) = u_i - u_{a(i)}$ , where  $l(i)$  and  $a(i)$  denote the nearest neighbors of  $i$ , to the left and above, respectively. The operators  $\Delta_i^{hh}(\mathbf{x})$ ,  $\Delta_i^{vv}(\mathbf{x})$ ,  $\Delta_i^{hv}(\mathbf{x})$  correspond, respectively, to horizontal, vertical and horizontal-vertical second order differences, at pixel  $i$ , as suggested by [25].

The second regularization term considered is adapted to US TRF images modeled by GGD statistics. In this case, the regularization term becomes [19, 20]:

$$P(\mathbf{x}) = \|\mathbf{x}\|_p^p \quad (11)$$

where  $p$  is related to the shape parameter of the GGD. In this paper, we focus on shape parameters ranging from 1 to 2 ( $1 \leq p \leq 2$ ), thus including and generalizing the Laplacian and Gaussian statistics used in the US literature [16–18].

### E. Implementation Details

In this subsection, we detail each of the three steps of our ADMM-based compressive deconvolution method. While the following mathematical developments are given for  $P(\mathbf{x}) = \|\mathbf{x}\|_p^p$  (adapted to US images), our approach using a generalized total variation regularization is also detailed in Algorithm 1.

**Step 1** consists in solving:

$$\begin{aligned} \mathbf{z}^k = \underset{\mathbf{z} \in \mathbb{R}^{2N}}{\operatorname{argmin}} \quad & g(\mathbf{z}) - (\boldsymbol{\lambda}^{k-1})^t (B\mathbf{a}^{k-1} + C\mathbf{z}) \\ & + \frac{\beta}{2} \|B\mathbf{a}^{k-1} + C\mathbf{z}\|_2^2 \end{aligned} \quad (12)$$

Since  $\mathbf{z} = \begin{bmatrix} \mathbf{w} \\ \mathbf{x} \end{bmatrix}$ , this  $\mathbf{z}$ -problem can be further divided into two subproblems.

*Step 1.1* aims at solving:

---

**Algorithm 1** The Alternating Direction Method of Multipliers for Solving (3)

---

**Require:**  $\mathbf{a}^0, \boldsymbol{\lambda}^0, \alpha, \mu, \beta$ 
**Ensure:**  $\mathbf{x}$ 

```

1: while not converged do
2:   Step 1. Given  $\mathbf{a}^{k-1}$  and  $\boldsymbol{\lambda}^{k-1}$ , update  $\mathbf{z}^k$ 
3:   Step 1.1 update  $\mathbf{w}^k$  by using the proximal operator:
4:    $\mathbf{w}^k = prox_{\|\cdot\|_1}(\mathbf{a}^{k-1} - \frac{\boldsymbol{\lambda}_1^{k-1}}{\beta})$ 
5:   Step 1.2
6:   switch  $P(\mathbf{x})$  do
7:     case  $P(\mathbf{x}) = \sum_{d \in D} 2^{1-o(d)} \sum_i |\Delta_i^d(\mathbf{x})|^p$ 
8:       for  $l = 1, 2, \dots$  until a stopping criterion is met: do
9:         Update  $\mathbf{x}^{k,l}$  by calculating:
10:        
$$\mathbf{x}^{k,l} = \left[ \beta H^t H + \alpha p \sum_d 2^{1-o(d)} (\Delta^d)^t B_d^{k-1,l} (\Delta^d) \right]^{-1} \times [\beta H^t \Psi \mathbf{a}^{k-1} - H^t \boldsymbol{\lambda}_2^{k-1}] \quad [25]$$

11:         $v_{d,i}^{k,l+1} = [\Delta_i^d(\mathbf{x})^{k,l}]^2$ 
12:       end for
13:       case  $P(\mathbf{x}) = \|\mathbf{x}\|_2^2$ 
14:          $\mathbf{x}^k = [\beta H^t H + 2\alpha I_N]^{-1} \times [\beta H^t \Psi \mathbf{a}^{k-1} - H^t \boldsymbol{\lambda}_2^{k-1}]$ 
15:       case  $P(\mathbf{x}) = \|\mathbf{x}\|_p^p, p \in [1, 2)$ 
16:          $\mathbf{x}^k = prox_{\alpha \gamma \|\cdot\|_p^p / \beta} \{ \mathbf{x}^{k-1} - \gamma h'(\mathbf{x}^{k-1}) \}$ 
17:       Step 2. Given  $\mathbf{z}^k = \begin{bmatrix} \mathbf{w}^k \\ \mathbf{x}^k \end{bmatrix}$  and  $\boldsymbol{\lambda}^{k-1}$ , update  $\mathbf{a}^k$  by solving the following linear system
18:       
$$\mathbf{a}^k = (\frac{1}{\mu} A^t A + \beta I_N + \beta \Psi^t \Psi)^{-1} (\frac{1}{\mu} A^t \mathbf{y} + \boldsymbol{\lambda}_1^{k-1} + \Psi^t \boldsymbol{\lambda}_2^{k-1} + \beta \mathbf{w}^k + \beta \Psi^t H \mathbf{x}^k)$$

19:       Step 3. Given  $\mathbf{z}^k = \begin{bmatrix} \mathbf{w}^k \\ \mathbf{x}^k \end{bmatrix}$  and  $\mathbf{a}^k$ , update  $\boldsymbol{\lambda}^k$  by
20:       
$$\boldsymbol{\lambda}^k = \boldsymbol{\lambda}^{k-1} - \beta (B \mathbf{a}^k + C \mathbf{z}^k)$$

21: end while

```

---

$$\begin{aligned}
\mathbf{w}^k &= \underset{\mathbf{w} \in \mathbb{R}^N}{\operatorname{argmin}} \quad \|\mathbf{w}\|_1 - (\boldsymbol{\lambda}_1^{k-1})^t (\mathbf{a}^{k-1} - \mathbf{w}) \\
&\quad + \frac{\beta}{2} \|\mathbf{a}^{k-1} - \mathbf{w}\|_2^2 \\
\Leftrightarrow \mathbf{w}^k &= \underset{\mathbf{w} \in \mathbb{R}^N}{\operatorname{argmin}} \|\mathbf{w}\|_1 + \frac{\beta}{2} \|\mathbf{a}^{k-1} - \mathbf{w} - \frac{\boldsymbol{\lambda}_1^{k-1}}{\beta}\|_2^2 \\
\Leftrightarrow \mathbf{w}^k &= prox_{\|\cdot\|_1/\beta} \left( \mathbf{a}^{k-1} - \frac{\boldsymbol{\lambda}_1^{k-1}}{\beta} \right)
\end{aligned} \tag{13}$$

where  $prox$  stands for the proximal operator as proposed in [34–36]. The proximal operator of  $f$  is defined for  $x^0 \in \mathbb{R}^N$  by:

$$prox_f(x^0) = \underset{\mathbf{x} \in \mathbb{R}^N}{\operatorname{argmin}} \quad f(\mathbf{x}) + \frac{1}{2} \|\mathbf{x} - x^0\|_2^2 \tag{14}$$

The proximal operator of  $\|\cdot\|_1/\beta$  has been given explicitly in the literature (see e.g. [37]):

$$\begin{aligned} prox_{\|\cdot\|_1/\beta}(x^0) &= \underset{\mathbf{x} \in \mathbb{R}^N}{\operatorname{argmin}} \quad \| \mathbf{x} \|_1 + \frac{\beta}{2} \| \mathbf{x} - x^0 \|_2^2 \\ &= \max \left\{ |x^0| - \frac{1}{\beta}, 0 \right\} \frac{x^0}{|x^0|} \end{aligned} \quad (15)$$

Based on (15), the last line of eq. (13) becomes:

$$\begin{aligned} \mathbf{w}^k(i) &= \max \left\{ \left| \mathbf{a}^{k-1}(i) - \frac{\boldsymbol{\lambda}_1^{k-1}(i)}{\beta} \right| - \frac{1}{\beta}, 0 \right\} \\ &\quad \cdot \operatorname{sign} \left( \mathbf{a}^{k-1}(i) - \frac{\boldsymbol{\lambda}_1^{k-1}(i)}{\beta} \right) \end{aligned} \quad (16)$$

where  $i \in \{1, 2, \dots, N\}$  and  $\mathbf{w}(i)$  denotes the intensity value of pixel  $i$ .

*Step 1.2* consists in solving:

$$\begin{aligned} \mathbf{x}^k &= \underset{\mathbf{x} \in \mathbb{R}^N}{\operatorname{argmin}} \quad \alpha \| \mathbf{x} \|_p^p - \boldsymbol{\lambda}_2^{k-1} (\Psi \mathbf{a}^{k-1} - H \mathbf{x}) \\ &\quad + \frac{\beta}{2} \| \Psi \mathbf{a}^{k-1} - H \mathbf{x} \|_2^2 \end{aligned} \quad (17)$$

For  $p$  equal to 2, the minimization in (17) can be easily solved in the Fourier domain, as follows:

$$\mathbf{x}^k = [\beta H^t H + 2\alpha I_N]^{-1} \times [\beta H^t \Psi \mathbf{a}^{k-1} - H^t \boldsymbol{\lambda}_2^{k-1}] \quad (18)$$

For  $1 \leq p < 2$ , we propose to use the proximal operator to solve (17). In this case, eq. (17) will be equivalent to

$$\mathbf{x}^k = \underset{\mathbf{x} \in \mathbb{R}^N}{\operatorname{argmin}} \quad \alpha \| \mathbf{x} \|_p^p + \frac{\beta}{2} \| \Psi \mathbf{a}^{k-1} - H \mathbf{x} - \frac{\boldsymbol{\lambda}_2^{k-1}}{\beta} \|_2^2 \quad (19)$$

Denoting  $h(\mathbf{x}) = \frac{1}{2} \| \Psi \mathbf{a}^{k-1} - H \mathbf{x} - \frac{\boldsymbol{\lambda}_2^{k-1}}{\beta} \|_2^2$ , we can further approximate  $h(\mathbf{x})$  by

$$h'(\mathbf{x}^{k-1})(\mathbf{x} - \mathbf{x}^{k-1}) + \frac{1}{2\gamma} \| \mathbf{x} - \mathbf{x}^{k-1} \|_2^2 \quad (20)$$

where  $\gamma > 0$  is a parameter related to the Lipschitz constant [38] and  $h'(\mathbf{x}^{k-1})$  is the gradient of  $h(\mathbf{x})$  when  $\mathbf{x} = \mathbf{x}^{k-1}$ , which is equal to

$$h'(\mathbf{x}^{k-1}) = H^t(H\mathbf{x}^{k-1} - \Psi\mathbf{a}^{k-1} + \frac{\lambda_2^{k-1}}{\beta}) \quad (21)$$

By plugging (20) and (21) into (19), we obtain:

$$\begin{aligned} \mathbf{x}^k &\approx \underset{\mathbf{x} \in \mathbb{R}^N}{\operatorname{argmin}} \quad \alpha \|\mathbf{x}\|_p^p + \beta h'(\mathbf{x}^{k-1})(\mathbf{x} - \mathbf{x}^{k-1}) \\ &\quad + \frac{\beta}{2\gamma} \|\mathbf{x} - \mathbf{x}^{k-1}\|_2^2 \\ \Leftrightarrow \mathbf{x}^k &\approx \underset{\mathbf{x} \in \mathbb{R}^N}{\operatorname{argmin}} \quad \alpha \|\mathbf{x}\|_p^p + \frac{\beta}{2\gamma} \|\mathbf{x} - \mathbf{x}^{k-1} + \gamma h'(\mathbf{x}^{k-1})\|_2^2 \end{aligned} \quad (22)$$

According to the definition of the proximal operator, we can finally get

$$\mathbf{x}^k \approx \operatorname{prox}_{\alpha\gamma\|\cdot\|_p^p/\beta}\{\mathbf{x}^{k-1} - \gamma h'(\mathbf{x}^{k-1})\} \quad (23)$$

We should note that the proximal operator associated to  $\|\cdot\|_p^p$  has been given in [37].

$$\operatorname{prox}_{K|x|^p}(x^0) = \operatorname{sign}(x^0)q \quad (24)$$

where  $q \geq 0$  and

$$q + pKq^{p-1} = |x^0| \quad (25)$$

In our numerical implementation, we used Newton's method to obtain its numerical solution, *i.e.* the value of  $q$ .

**Step 2** aims at solving:

$$\begin{aligned} \mathbf{a}^k &= \underset{\mathbf{a} \in \mathbb{R}^N}{\operatorname{argmin}} \quad \frac{1}{2\mu} \|\mathbf{y} - A\mathbf{a}\|_2^2 - (\boldsymbol{\lambda}^{k-1})^t(B\mathbf{a} + C\mathbf{z}^k) \\ &\quad + \frac{\beta}{2} \|B\mathbf{a} + C\mathbf{z}^k\|_2^2 \\ \Leftrightarrow \mathbf{a}^k &= \left(\frac{1}{\mu} A^t A + \beta B^t B\right)^{-1} \left(\frac{1}{\mu} A^t \mathbf{y} + B^t \boldsymbol{\lambda}^{k-1} - \beta B^t C \mathbf{z}^k\right) \\ &= \left(\frac{1}{\mu} A^t A + \beta I_N + \beta \Psi^t \Psi\right)^{-1} \left(\frac{1}{\mu} A^t \mathbf{y} + \boldsymbol{\lambda}_1^{k-1} + \Psi^t \boldsymbol{\lambda}_2^{k-1} \right. \\ &\quad \left. + \beta \mathbf{w}^k + \beta \Psi^t H \mathbf{x}^k\right) \end{aligned} \quad (26)$$

The formula above is equivalent to solving an  $N \times N$  linear system or inverting an  $N \times N$  matrix. However, since the sparse basis  $\Psi$  considered is orthogonal (e.g. the wavelet transform), it can be reduced to solving a smaller  $M \times M$  linear system or inverting an  $M \times M$  matrix by exploiting the Sherman-Morrison-Woodbury inversion matrix lemma [39]:

$$(\beta_1 I_N + \beta_2 A^t A)^{-1} = \frac{1}{\beta_1} I_N - \frac{\beta_2}{\beta_1} A^t (\beta_1 I_M + \beta_2 A A^t)^{-1} A \quad (27)$$

In this paper, without loss of generality, we considered the compressive sampling matrix  $\Phi$  as a Structurally Random Matrix (SRM) [40]. Therefore,  $A$  was formed by randomly taking a subset of rows from orthonormal transform matrices, that is,  $A A^t = I_M$ . As a consequence, there is no need to solve a linear system and the main computational cost consists into two matrix-vector multiplications per iteration.

**Step 3** consists in solving:

$$\boldsymbol{\lambda}^k = \boldsymbol{\lambda}^{k-1} - \beta(B\mathbf{a}^k + C\mathbf{z}^k) \quad (28)$$

The proposed optimization routine is summarized in Algorithm 1.

### III. RESULTS

The performance of the proposed compressive deconvolution method are evaluated on several simulated and experimental data sets. First, we compare our approach with the one in [25] on the standard Shepp-Logan phantom. Second, we test our algorithm on simulated US images for different  $l_p$  norm optimizations and compare it against the intuitive sequential method explained at the beginning of section II. Finally, compressive deconvolution results on two *in vivo* ultrasound images are presented.

#### A. Results on Shepp-Logan phantom

The aim of the first experiment is to evaluate the performance of the proposed approach compared to a recent compressive deconvolution technique reported in [25], referred as CD\_Amizic hereafter. The comparison results are obtained on the standard  $256 \times 256$  Shepp-Logan phantom. The measurements have been generated in a similar manner as in [25], *i.e.* the original image was normalized, degraded by a  $2D$  Gaussian PSF with a 5-pixel variance, projected onto a structured random matrix (SRM) to generate the CS measurements and corrupted by an additive Gaussian noise. We should remark that in [25] the

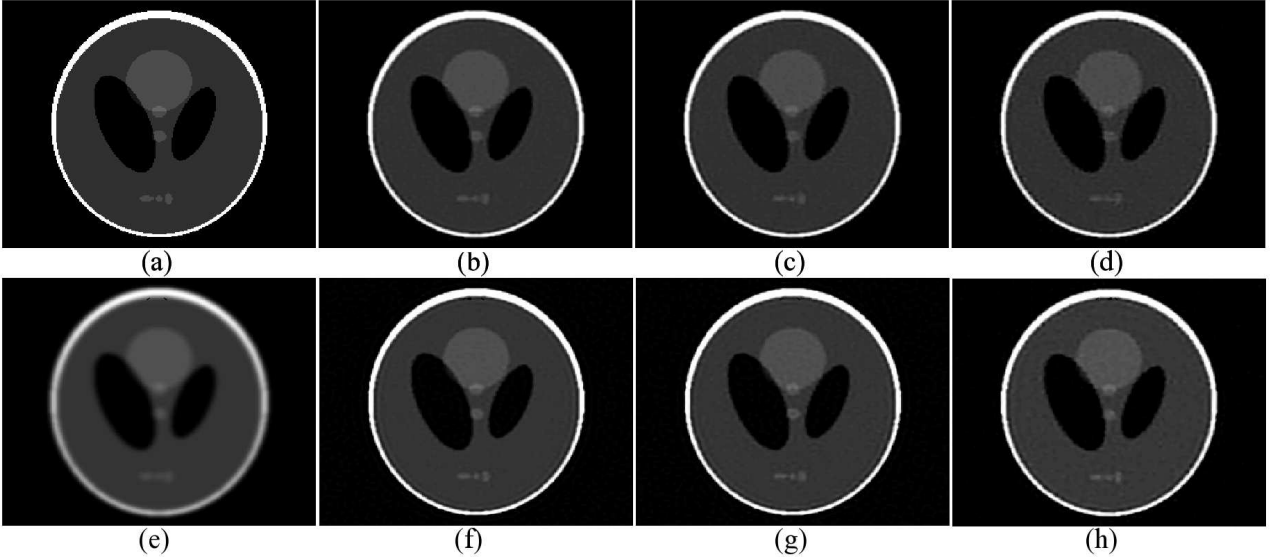


Fig. 1: Shepp-logan image and its compressive deconvolution results for a SNR of 40dB. (a) Original image, (e) Blurred image, (b,c,d) Compressive deconvolution results with CD\_Amizic for CS ratios of 0.8, 0.6 and 0.4, (f,g,h) Compressive deconvolution results with the proposed method for CS ratios of 0.8, 0.6 and 0.4.

compressed measurements were generated using a Gaussian random matrix. However, we have found that the reconstruction results with CD\_Amizic are equivalent when using a SRM. Both methods were based on the same priors: the generalized total variation in eq. (10) to model the image to be estimated and the 3-level Haar wavelet transform as sparsifying basis  $\Psi$ . With our method, the hyperparameters were set to  $\{\alpha, \mu, \beta\} = \{10^{-1}, 10^{-5}, 10^2\}$ . The same hyperparameters as reported in [25] were used for CD\_Amizic. Both algorithms used the same stopping criteria and the same PSF preliminary estimated offline.

Fig.1 shows the original Shepp-Logan image, its blurred version and a series of compressive deconvolution reconstructions using both our method and CD\_Amizic for CS ratios running from 0.4 to 0.8 and a SNR of 40 dB. The results were quantitatively evaluated using the standard peak signal-to-noise ratio (PSNR) defined as

$$PSNR = 10 \log_{10} \frac{NL^2}{\| \mathbf{x} - \hat{\mathbf{x}} \|^2} \quad (29)$$

where  $\mathbf{x}$  and  $\hat{\mathbf{x}}$  are the original and reconstructed images, and the constant L represents the maximum intensity value in  $\mathbf{x}$ .

Table.I regroups the PSNRs obtained with our method and with CD\_Amizic for two SNRs and for four CS ratios from 0.2 to 0.4. In each case, the reported PSNRs are the mean values of 10 experiments. We

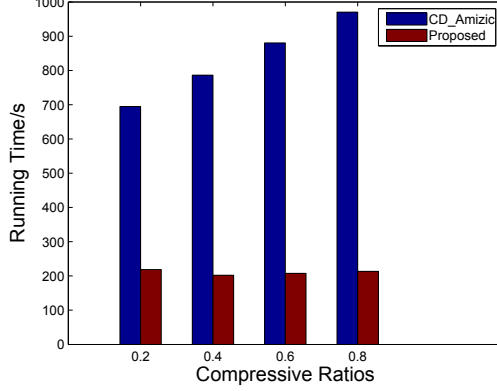


Fig. 2: Mean reconstruction running time for 10 experiments conducted for each CS ratio for a SNR of 40 dB.

may observe that our method outperforms CD\_Amizic in all the cases, allowing a PSNR improvement of roughly 1 to 2 dB. Moreover, Fig.2 shows the computational times with CD\_Amizic and the proposed method, obtained with Matlab implementations (for CD\_Amizic, the original code provided by the authors of [25] has been employed) on a standard desktop computer (Intel Xeon CPU E5620 @ 2.40GHz, 4.00G RAM). We notice that our approach is roughly four times less time consuming than CD\_Amizic.

TABLE I: PSNR assessment for Shepp-Logan phantom

SNR	CS ratios	20%	40%	60%	80%
40dB	CD_Amizic	22.52	24.74	25.18	25.40
	Proposed method	<b>24.09</b>	<b>25.38</b>	<b>26.26</b>	<b>26.91</b>
30dB	CD_Amizic	22.10	23.87	24.27	24.44
	Proposed method	<b>23.92</b>	<b>25.12</b>	<b>25.82</b>	<b>26.33</b>

The objective of the next experiment is to confirm that the  $l_p$ -norm regularization term in eq. (11) is further adapted to US images than the generalized total variation used in [25]. Thus, we modified the Shepp-Logan phantom in order to simulate the speckle noise that degrades in practice the US images. For this, we followed the procedure classically used in US imaging. First, scatters at uniformly random locations have been generated, with amplitudes distributed according to a zero-mean generalized Gaussian distribution (GGD) with the shape parameter set to 1.3 and the scale parameter equal to 1. The scatterer amplitudes were further multiplied by the values of the original Shepp-Logan phantom pixels located at the closest positions to the scatterers. The resulting image, mimicking the tissue reflectivity function (TRF) in US imaging, is shown in Fig.3(a). The blurred image in Fig.3(b) was obtained by 2D convolution between the TRF and a PSF generated with Field II [41], a state-of-the-art simulator in US imaging. It corresponds to a 3.5 MHz linear probe, sampled in the axial direction at 20 MHz. The compressive measurements

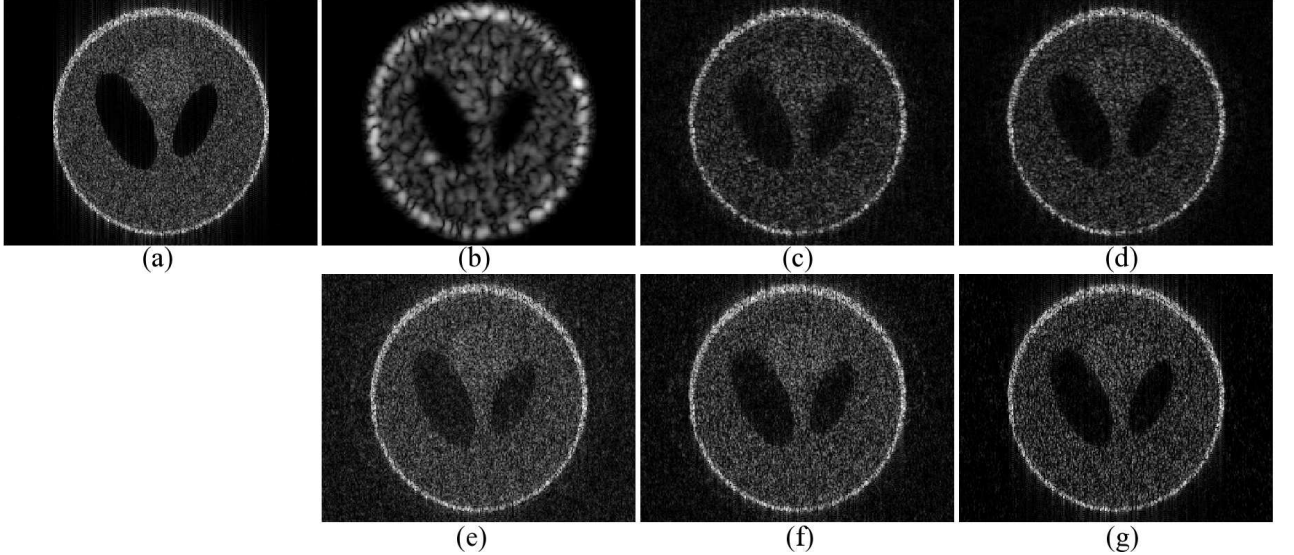


Fig. 3: Reconstruction results for SNR = 40dB and a CS ratio of 0.6. (a) Modified Shepp-Logan phantom containing random scatters (TRF), (b) Degraded image by convolution with a simulated US PSF, (c) Reconstruction result with CD\_Amizic, (d) Reconstruction result with the proposed method using a generalized TV prior (ADMM\_GTV), (e, f, g) Reconstruction results with the proposed method using an  $l_p$ -norm prior, for  $p$  equal to 1.5, 1.3 and 1 (ADMM\_L1.5, ADMM\_L1.3 and ADMM\_L1).

were obtained by projecting the blurred image onto SRM and by adding a Gaussian noise corresponding to a SNR of 40 dB.

The reconstruction results are evaluated using the PSNR and the Structural Similarity (SSIM) [42], extensively used in US imaging and defined as

$$SSIM = \frac{(2\mu_x\mu_{\hat{x}} + c_1)(2\sigma_{x\hat{x}} + c_2)}{(\mu_x^2 + \mu_{\hat{x}}^2 + c_1)(\sigma_x^2 + \sigma_{\hat{x}}^2 + c_2)} \quad (30)$$

where  $x$  and  $\hat{x}$  are the original and reconstructed images,  $\mu_x$ ,  $\mu_{\hat{x}}$ ,  $\sigma_x$  and  $\sigma_{\hat{x}}$  are the mean and variance values of  $x$  and  $\hat{x}$ ,  $\sigma_{x\hat{x}}$  is the covariance between  $x$  and  $\hat{x}$ ;  $c_1 = (k_1 L)^2$  and  $c_2 = (k_2 L)^2$  are two variables aiming at stabilizing the division with weak denominator,  $L$  is the dynamic range of the pixel-values and  $k_1$ ,  $k_2$  are constants. Herein,  $L = 1$ ,  $k_1 = 0.01$  and  $k_2 = 0.03$ .

Reconstruction results for a CS ratio of 0.6 are shown in Fig.3. They were obtained with: CD\_Amizic [25], the proposed method using the generalized TV prior in eq. (10) (denoted by ADMM\_GTV) and the proposed method using the  $l_p$ -norm in eq. (11), for  $p$  equal to 1.5, 1.3 and 1 (denoted respectively by ADMM\_L1.5, ADMM\_L1.3 and ADMM\_L1). All the hyperparameters were set to their best possible values by cross-validation. For CD\_Amizic,  $\{\beta, \alpha, \eta, \tau\} = \{10^7, 1, 10^4, 10^2\}$ . For ADMM\_GTV  $\{\mu, \alpha, \beta\} = \{10^{-5}, 2 \times 10^{-1}, 10^2\}$  and for the proposed method with  $l_p$ -norms,  $\{\mu, \alpha, \beta, \gamma\} = \{10^{-5}, 2 \times$

TABLE II: Quantitative results for the modified Shepp-Logan phantom with US speckle (SNR = 40dB)

CS ratios		CD_Amizic	ADMM_GTV	ADMM_L1.5	ADMM_L1.3	ADMM_L1
80%	PSNR	30.82	31.11	32.23	<b>32.32</b>	32.05
	SSIM	83.24	85.03	86.44	<b>88.77</b>	87.70
60%	PSNR	29.68	29.83	31.27	<b>31.50</b>	31.32
	SSIM	74.58	77.83	82.26	<b>86.03</b>	85.64
40%	PSNR	26.76	28.11	29.58	30.04	<b>30.12</b>
	SSIM	43.43	61.46	73.88	79.95	<b>81.75</b>
20%	PSNR	20.22	21.53	26.81	27.29	<b>28.20</b>
	SSIM	8.35	12.77	51.70	62.93	<b>72.34</b>

$10^{-1}, 10^1, 3 \times 10^{-2}\}$ . The quantitative results for different CS ratios are regrouped in Table.II. They confirm that the  $l_p$ -norm is better adapted to recover the TRF in US imaging than the generalized TV. The difference between the two priors is further accentuated when the CS ratio decreases.

Keeping in mind that the generalized TV prior is not well suited to model the TRF in US imaging, we did not use CD\_Amizic in the following sections dealing with simulated and experimental US images. Moreover, the proposed method was only evaluated in its  $l_p$ -norm minimization form.

### B. Results on simulated ultrasound images

In this section, we compared the compressive deconvolution results with our method to those obtained with a sequential approach. The latter recovers in a first step the blurred US image from the CS measurements and reconstructs in a second step the TRF by deconvolution.

Two ultrasound data sets were generated, as shown in Figures 4 and 5. They were obtained by 2D convolution between the PSFs and the TRFs. For the first simulated image, the same PSF as in the previous section was simulated and the TRF corresponds to a simple medium representing a round hypoechoic inclusion into a homogeneous medium. The scatter amplitudes were random variables distributed according to a GGD with the shape parameter set to 1. The second data set is one of the examples proposed by the Field II simulator [41], mimicking a kidney tissue. The PSF was also generated with Field II corresponding to a 4 MHz central frequency and a axial sampling frequency of 40 MHz. The shape parameter of the GGD used to generate the scatterer amplitudes was set to 1.5 and the number of scatterers was considered sufficiently large ( $10^6$ ) to ensure fully developed speckle.

With the sequential approach, YALL1 [43] was used to process the CS reconstruction following the minimization in eq. (3). The deconvolution step was processed using the Forward-Backward Splitting

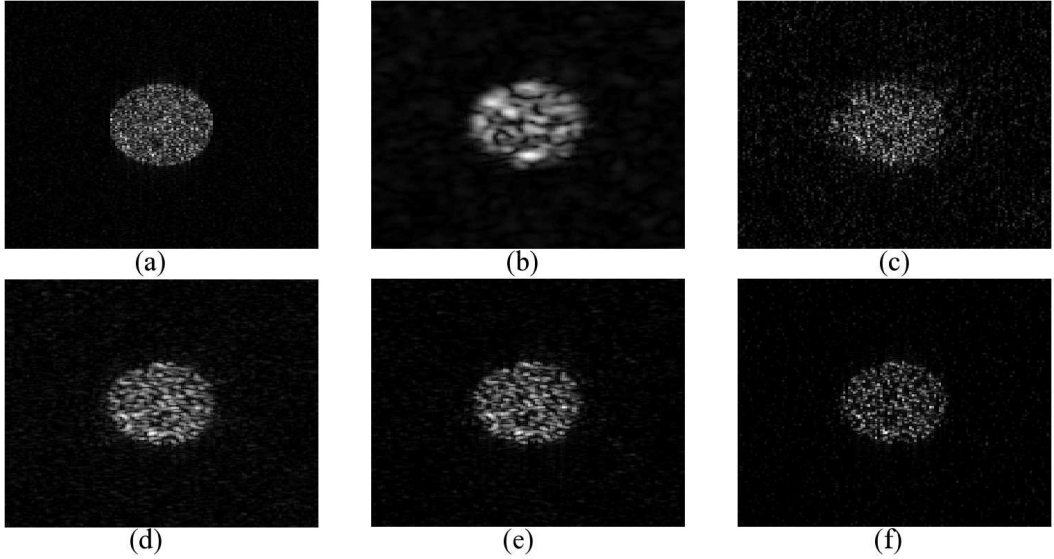


Fig. 4: Simulated US image and its compressive deconvolution results for a CS ratio of 0.4 and a SNR of 40 dB. (a) Original tissue reflectivity function, (b) Simulated US image, (c) Results using the sequential method, (d, e, f) Results with the proposed method for  $p$  equal to 1.5, 1.3 and 1 respectively.

method [44, 45]. Both the CS reconstruction and the deconvolution procedures were performed with the same priors as the proposed compressive deconvolution approach.

All the hyperparameters were set to their best possible values by cross-validation. The hyperparameters with our approach were set to  $\{\mu, \alpha, \beta, \gamma\} = \{10^{-5}, 2 \times 10^{-1}, 1, 10^{-2}\}$  for the first image and  $\{\mu, \alpha, \beta, \gamma\} = \{10^{-5}, 2 \times 10^{-1}, 1 \times 10^3, 10^{-4}\}$  for the second image. The algorithm stops when the convergence criterion  $\|\mathbf{x}^k - \mathbf{x}^{k-1}\| / \|\mathbf{x}^{k-1}\| < 1e^{-3}$  is satisfied.

The quantitative results in Tables III and IV show that the proposed method outperforms the sequential approach, for all the CS ratios and values of  $p$  considered. They confirm the visual impression given by Figures 4 and 5. We should remark that for the first simulated data set, the  $l_1$ -norm gives the best result. This may be explained by the simple geometry of the simulated TRF, namely its sparse appearance. The second data set, more realistic and more representative of experimental situations, shows the interest of using different values of  $p$ . It confirms the generality interest of the proposed method, namely its flexibility in the choice of TRF priors.

### C. In vivo study

In this section, we tested our method with two *in vivo* data sets. The experimental data were acquired with a 20 MHz single-element US probe on a mouse bladder (first example) and kidney (second example). Unlike the simulated cases studied previously, the PSF is not known in these experiments and has to be

TABLE III: Quantitative results for the US image in Figure 4 (SNR = 40dB)

CS Ratios		Sequential	Proposed ( $l_{1.5}$ )	Proposed ( $l_{1.3}$ )	Proposed ( $l_1$ )
80%	PSNR	26.50	24.74	25.29	<b>26.82</b>
	SSIM	75.01	73.91	77.66	<b>79.45</b>
60%	PSNR	25.96	24.44	24.74	<b>26.03</b>
	SSIM	68.59	69.37	74.72	<b>76.26</b>
40%	PSNR	23.38	24.21	24.57	<b>25.28</b>
	SSIM	47.60	62.58	71.86	<b>72.78</b>
20%	PSNR	21.10	23.72	24.42	<b>24.77</b>
	SSIM	36.07	50.34	66.48	<b>70.44</b>

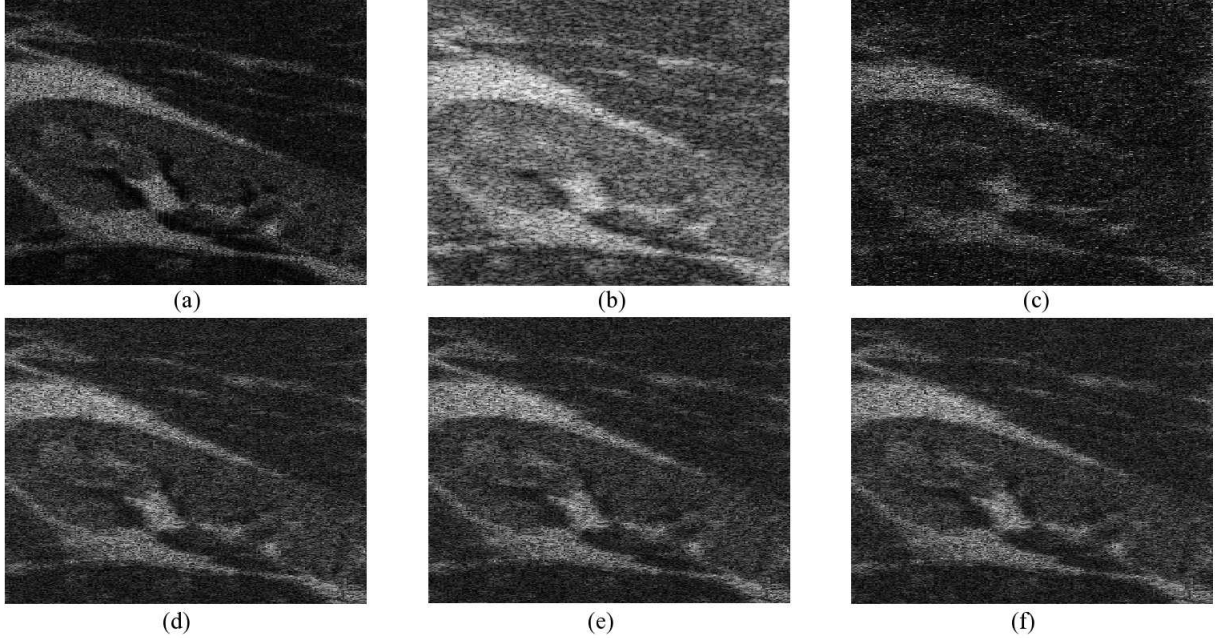
Fig. 5: Simulated kidney image and its compressive deconvolution results for a CS ratio of 0.2 and a SNR of 40dB. (a) Original tissue reflectivity function, (b) Simulated US image, (c) Results using the sequential method, (d, e, f) Results with the proposed method for  $p$  equal to 1.5, 1.3 and 1 respectively.

TABLE IV: Quantitative results for the US image in Figure 5 (SNR = 40dB)

CS Ratios		Sequential	Proposed ( $l_{1.5}$ )	Proposed ( $l_{1.3}$ )	Proposed ( $l_1$ )
80%	PSNR	26.06	26.71	<b>26.72</b>	26.69
	SSIM	45.99	56.81	<b>56.84</b>	56.71
60%	PSNR	25.44	<b>26.38</b>	26.31	26.29
	SSIM	38.86	<b>54.14</b>	53.90	53.80
40%	PSNR	25.37	25.89	25.95	<b>25.97</b>
	SSIM	34.61	50.22	50.51	<b>50.61</b>
20%	PSNR	24.96	<b>25.22</b>	25.20	25.12
	SSIM	30.89	<b>41.41</b>	41.32	40.97

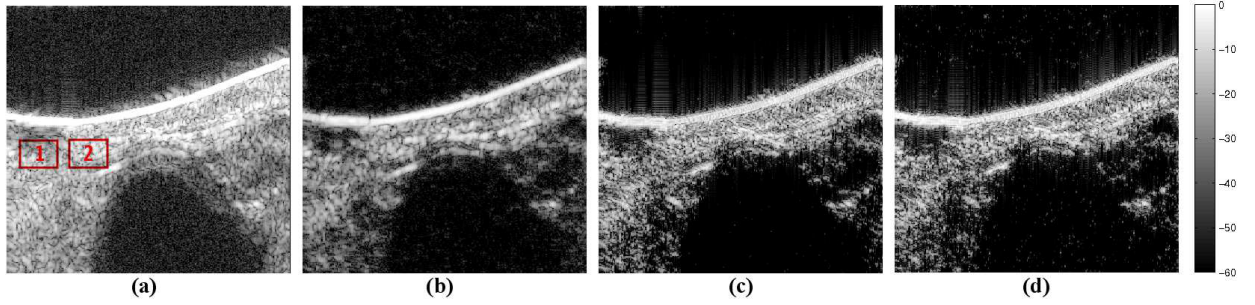


Fig. 6: From left to right, the original *in vivo* image and its compressive deconvolution results for CS ratios of 0.8, 0.6 and 0.4 respectively with  $p = 1$ .

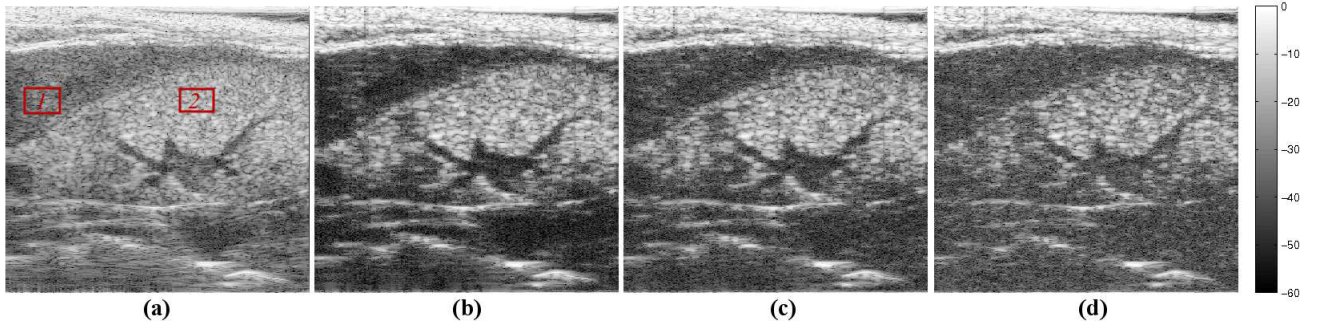


Fig. 7: From left to right, the original *in vivo* image and its compressive deconvolution results for CS ratios of 0.8, 0.6 and 0.4 respectively with  $p = 1.5$ .

estimated from the data. In this paper, the PSF estimation method presented in [33] has been adopted. The compressive deconvolution results are shown in Figures 6 and 7 for different CS ratios.

Given that the true TRF is not known in experimental conditions, the quality of the reconstruction results is evaluated using the contrast-to-noise ratio (CNR) [46], defined as

$$CNR = \frac{|\mu_1 - \mu_2|}{\sqrt{\sigma_1^2 + \sigma_2^2}} \quad (31)$$

where  $\mu_1$  and  $\mu_2$  are the mean of pixels located in two regions extracted from the image while  $\sigma_1$  and  $\sigma_2$  are the standard deviations of the same blocks. The two regions selected for the computation of the CNR are highlighted by the two red rectangles in Figures 6(a) and 7(a). Table. V gives the CNR assessment for these two *in vivo* data sets with different CS ratios and  $p$  values. Given the sparse appearance of the bladder image in Fig. 6(a), the best result was obtained for  $p$  equal to 1. However, the complexity of the tissue structures in the kidney image in Fig. 7 results into better results for  $p$  larger than 1. Nevertheless, both the visual impression and the CNR results show the ability of our method to both recover the image from compressive measurements and to improve its contrast compared to the standard US image. In

particular, we may remark the improved contrast of the structures inside the kidney on our reconstructed images compared to the original one.

TABLE V: CNR assessment for *in vivo* data

Figure	Original CNR	<i>p</i> values	CS ratios		
			80%	60%	40%
Fig.6	1.106	<i>p</i> = 1	<b>1.546</b>	<b>1.367</b>	<b>1.333</b>
		<i>p</i> = 1.5	1.424	1.304	1.287
Fig.7	1,316	<i>p</i> = 1	<b>2.162</b>	1.895	1.434
		<i>p</i> = 1.5	2.082	<b>1.905</b>	<b>1.451</b>

#### IV. CONCLUSION

This paper introduced an ADMM-based compressive deconvolution framework for ultrasound imaging systems. The main benefit of our approach is its ability to reconstruct enhanced ultrasound RF images from compressed measurements, by inverting a linear model combining random projections and 2D convolution. Simulation results on the standard Shepp-Logan phantom show the superiority of our method, both in accuracy and in computational time, over a recently published compressive deconvolution approach. Moreover, we show that the proposed joint CS and deconvolution approach is more robust than an intuitive technique consisting of first reconstructing the RF data and second deconvolving it. Finally, promising results on *in vivo* data demonstrate the effectiveness of our approach in practical situations. Our future work includes: I) the consideration of blind deconvolution techniques able to estimate (update) the PSF during the reconstruction process, II) automatic techniques for choosing the optimal parameter *p* used to regularize the tissue reflectivity function, III) extend our method to 3D ultrasound imaging, IV) evaluate other existing setups to obtain the random compressed measurements, V) evaluate our approach on more experimental data.

#### ACKNOWLEDGMENT

The authors would like to thank Prof. Rafael Molina for providing the compressive deconvolution code used for comparison purpose in this paper. This work was partially supported by ANR-11-LABX-0040-CIMI within the program ANR-11-IDEX-0002-02 of the University of Toulouse and CSC (Chinese Scholarship Council).

#### REFERENCES

[1] T. L. Szabo, *Diagnostic ultrasound imaging: inside out*. Academic Press, 2004.

- [2] M. Tanter and M. Fink, “Ultrafast imaging in biomedical ultrasound,” *Ultrasonics, Ferroelectrics, and Frequency Control, IEEE Transactions on*, vol. 61, no. 1, pp. 102–119, January 2014.
- [3] A. Achim, B. Buxton, G. Tzagkarakis, and P. Tsakalides, “Compressive sensing for ultrasound rf echoes using a-stable distributions,” in *Engineering in Medicine and Biology Society (EMBC), 2010 Annual International Conference of the IEEE*. IEEE, 2010, pp. 4304–4307.
- [4] C. Quinsac, A. Basarab, and D. Kouamé, “Frequency domain compressive sampling for ultrasound imaging,” *Advances in Acoustics and Vibration*, 2012.
- [5] T. Chernyakova and Y. C. Eldar, “Fourier-domain beamforming: the path to compressed ultrasound imaging,” *Ultrasonics, Ferroelectrics, and Frequency Control, IEEE Transactions on*, vol. 61, no. 8, pp. 1252–1267, 2014.
- [6] H. Liebgott, A. Basarab, D. Kouamé, O. Bernard, and D. Friboulet, “Compressive sensing in medical ultrasound,” in *Ultrasonics Symposium (IUS), 2012 IEEE International*. IEEE, 2012, pp. 1–6.
- [7] H. Liebgott, R. Prost, and D. Friboulet, “Pre-beamformed rf signal reconstruction in medical ultrasound using compressive sensing,” *Ultrasonics*, vol. 53, no. 2, pp. 525–533, 2013.
- [8] M. F. Schiffner and G. Schmitz, “Pulse-echo ultrasound imaging combining compressed sensing and the fast multipole method,” in *Ultrasonics Symposium (IUS), 2014 IEEE International*. IEEE, 2014, pp. 2205–2208.
- [9] J. Richy, H. Liebgott, R. Prost, and D. Friboulet, “Blood velocity estimation using compressed sensing,” in *IEEE International Ultrasonics Symposium*, Orlando (USA), 2011, pp. 1427–1430.
- [10] D. L. Donoho, “Compressed sensing,” *Information Theory, IEEE Transactions on*, vol. 52, no. 4, pp. 1289–1306, 2006.
- [11] E. J. Candès, J. Romberg, and T. Tao, “Robust uncertainty principles: Exact signal reconstruction from highly incomplete frequency information,” *Information Theory, IEEE Transactions on*, vol. 52, no. 2, pp. 489–509, 2006.
- [12] E. J. Candès and M. B. Wakin, “An introduction to compressive sampling,” *Signal Processing Magazine, IEEE*, vol. 25, no. 2, pp. 21–30, 2008.
- [13] O. Lorintiu, H. Liebgott, M. Alessandrini, O. Bernard, and D. Friboulet, “Compressed sensing reconstruction of 3d ultrasound data using dictionary learning and line-wise subsampling,” *IEEE Transactions on Medical Imaging*, vol. accepted, 2015.
- [14] N. Dobigeon, A. Basarab, D. Kouamé, and J.-Y. Tourneret, “Regularized bayesian compressed sensing

in ultrasound imaging,” in *Signal Processing Conference (EUSIPCO), 2012 Proceedings of the 20th European*. IEEE, 2012, pp. 2600–2604.

[15] A. Basarab, A. Achim, and D. Kouamé, “Medical ultrasound image reconstruction using compressive sampling and iota $\rho$ -norm minimization,” in *SPIE Medical Imaging*. International Society for Optics and Photonics, 2014, pp. 90 401H–90 401H.

[16] T. Taxt and J. Strand, “Two-dimensional noise-robust blind deconvolution of ultrasound images,” *Ultrasonics, Ferroelectrics and Frequency Control, IEEE Transactions on*, vol. 48, no. 4, pp. 861–866, 2001.

[17] O. Michailovich and A. Tannenbaum, “Blind deconvolution of medical ultrasound images: A parametric inverse filtering approach,” *IEEE transactions on image processing: a publication of the IEEE Signal Processing Society*, vol. 16, no. 12, p. 3005, 2007.

[18] R. Morin, S. Bidon, A. Basarab, and D. Kouame, “Semi-blind deconvolution for resolution enhancement in ultrasound imaging,” in *Image Processing (ICIP), 2013 20th IEEE International Conference on*, Sept 2013, pp. 1413–1417.

[19] N. Zhao, A. Basarab, D. Kouamé, and J.-Y. Tourneret, “Restoration of ultrasound images using a hierarchical bayesian model with a generalized gaussian prior,” in *in Proc. Int. Conf. Image Process.(ICIP2014), Paris, France*, 2014.

[20] M. Alessandrini, S. Maggio, J. Porée, L. De Marchi, N. Speciale, E. Franceschini, O. Bernard, and O. Basset, “A restoration framework for ultrasonic tissue characterization,” *Ultrasonics, Ferroelectrics, and Frequency Control, IEEE Transactions on*, vol. 58, no. 11, pp. 2344–2360, 2011.

[21] J. A. Jensen, J. Mathorne, T. Gravesen, and B. Stage, “Deconvolution of in vivo ultrasound b-mode images,” *Ultrasonic Imaging*, vol. 15, no. 2, pp. 122–133, 1993.

[22] J. Ma and F.-X. Le Dimet, “Deblurring from highly incomplete measurements for remote sensing,” *Geoscience and Remote Sensing, IEEE Transactions on*, vol. 47, no. 3, pp. 792–802, 2009.

[23] L. Xiao, J. Shao, L. Huang, and Z. Wei, “Compounded regularization and fast algorithm for compressive sensing deconvolution,” in *Image and Graphics (ICIG), 2011 Sixth International Conference on*. IEEE, 2011, pp. 616–621.

[24] M. Zhao and V. Saligrama, “On compressed blind de-convolution of filtered sparse processes,” in *Acoustics Speech and Signal Processing (ICASSP), 2010 IEEE International Conference on*. IEEE, 2010, pp. 4038–4041.

- [25] B. Amizic, L. Spinoulas, R. Molina, and A. K. Katsaggelos, “Compressive blind image deconvolution,” *Image Processing, IEEE Transactions on*, vol. 22, no. 10, pp. 3994–4006, 2013.
- [26] L. Spinoulas, B. Amizic, M. Vega, R. Molina, and A. K. Katsaggelos, “Simultaneous bayesian compressive sensing and blind deconvolution,” in *Signal Processing Conference (EUSIPCO), 2012 Proceedings of the 20th European*. IEEE, 2012, pp. 1414–1418.
- [27] C. Hegde and R. G. Baraniuk, “Compressive sensing of streams of pulses,” in *Communication, Control, and Computing, 2009. Allerton 2009. 47th Annual Allerton Conference on*. IEEE, 2009, pp. 44–51.
- [28] C. Hegde and R. Baraniuk, “Sampling and recovery of pulse streams,” *Signal Processing, IEEE Transactions on*, vol. 59, no. 4, pp. 1505–1517, April 2011.
- [29] S. Boyd, N. Parikh, E. Chu, B. Peleato, and J. Eckstein, “Distributed optimization and statistical learning via the alternating direction method of multipliers,” *Found. Trends Mach. Learn.*, vol. 3, no. 1, pp. 1–122, Jan. 2011. [Online]. Available: <http://dx.doi.org/10.1561/2200000016>
- [30] X. Zhao, C. Chen, and M. Ng, “Alternating direction method of multipliers for nonlinear image restoration problems,” *Image Processing, IEEE Transactions on*, vol. 24, no. 1, pp. 33–43, Jan 2015.
- [31] R. Jirik and T. Taxt, “Two-dimensional blind bayesian deconvolution of medical ultrasound images,” *Ultrasonics, Ferroelectrics, and Frequency Control, IEEE Transactions on*, vol. 55, no. 10, pp. 2140–2153, 2008.
- [32] C. Yu, C. Zhang, and L. Xie, “A blind deconvolution approach to ultrasound imaging,” *Ultrasonics, Ferroelectrics, and Frequency Control, IEEE Transactions on*, vol. 59, no. 2, pp. 271–280, 2012.
- [33] O. V. Michailovich and D. Adam, “A novel approach to the 2-d blind deconvolution problem in medical ultrasound,” *Medical Imaging, IEEE Transactions on*, vol. 24, no. 1, pp. 86–104, 2005.
- [34] J.-C. Pesquet and N. Pustelnik, “A parallel inertial proximal optimization method,” *Pacific Journal of Optimization*, vol. 8, no. 2, pp. 273–305, 2012.
- [35] N. Pustelnik, C. Chaux, and J.-C. Pesquet, “Parallel proximal algorithm for image restoration using hybrid regularization,” *Image Processing, IEEE Transactions on*, vol. 20, no. 9, pp. 2450–2462, 2011.
- [36] N. Pustelnik, J. Pesquet, and C. Chaux, “Relaxing tight frame condition in parallel proximal methods for signal restoration,” *Signal Processing, IEEE Transactions on*, vol. 60, no. 2, pp. 968–973, 2012.
- [37] P. L. Combettes and J.-C. Pesquet, “Proximal splitting methods in signal processing,” in *Fixed-point algorithms for inverse problems in science and engineering*. Springer, 2011, pp. 185–212.

- [38] E. Chouzenoux, J.-C. Pesquet, and A. Repetti, “Variable metric forward–backward algorithm for minimizing the sum of a differentiable function and a convex function,” *Journal of Optimization Theory and Applications*, vol. 162, no. 1, pp. 107–132, 2014.
- [39] W. Deng, W. Yin, and Y. Zhang, “Group sparse optimization by alternating direction method,” vol. 8858, 2013, pp. 88 580R–88 580R–15. [Online]. Available: <http://dx.doi.org/10.1117/12.2024410>
- [40] T. T. Do, L. Gan, N. H. Nguyen, and T. D. Tran, “Fast and efficient compressive sensing using structurally random matrices,” *Signal Processing, IEEE Transactions on*, vol. 60, no. 1, pp. 139–154, 2012.
- [41] J. A. Jensen, “A model for the propagation and scattering of ultrasound in tissue,” *Acoustical Society of America. Journal*, vol. 89, no. 1, pp. 182–190, 1991.
- [42] Z. Wang, A. C. Bovik, H. R. Sheikh, and E. P. Simoncelli, “Image quality assessment: from error visibility to structural similarity,” *Image Processing, IEEE Transactions on*, vol. 13, no. 4, pp. 600–612, 2004.
- [43] J. Yang and Y. Zhang, “Alternating direction algorithms for 11-problems in compressive sensing,” *SIAM journal on scientific computing*, vol. 33, no. 1, pp. 250–278, 2011.
- [44] P. L. Combettes and V. R. Wajs, “Signal recovery by proximal forward-backward splitting,” *Multiscale Modeling & Simulation*, vol. 4, no. 4, pp. 1168–1200, 2005.
- [45] H. Raguet, J. Fadili, and G. Peyré, “A generalized forward-backward splitting,” *SIAM Journal on Imaging Sciences*, vol. 6, no. 3, pp. 1199–1226, 2013.
- [46] A. Lyshchik, T. Higashi, R. Asato, S. Tanaka, J. Ito, M. Hiraoka, A. Brill, T. Saga, and K. Togashi, “Elastic moduli of thyroid tissues under compression,” *Ultrasonic imaging*, vol. 27, no. 2, pp. 101–110, 2005.